The 2025 World Congress on
Advances in Structural Engineering and Mechanics (ASEM25)
BEXCO, Busan, Korea, August 11-14, 2025

Finite element model construction and seismic performance analysis of grottoes based on point cloud datas

Jun-Feng Lu[1)], Yan-Zhao Liu[2)], *Yi-Feng Wu[3)], Ai-Qun Li[4)], Yang Deng[5)]

[1), 2), 3), 4), 5)] *School of Civil and Transportation Engineering, Beijing University of Civil Engineering and Architecture, Beijing 100044, China*
[1)] 18510416133@163.com
[2)] 1839431336@qq.com
[3)] wuyifeng@bucea.edu.cn
[4)] liaiqun@bucea.edu.cn
[5)] dengyang@bucea.edu.cn

ABSTRACT

To delve into the seismic performance of grottoes, an inverse modeling method based on point cloud data is proposed. Based on the 3D laser scanning data of a grotto, the establishment of a high - precision 3D finite element analysis model for a complex grotto is achieved, facilitating the transformation from a physical entity in the real - world space to its virtual representation. Based on ABAQUS, the stress-strain characteristics, acceleration and displacement response of the grotto body under self-weight and X-direction earthquake were analyzed. The results indicate that the grotto remains in an elastic state under self - weight and small earthquakes; the grotto body experiences plastic deformation and tensile damage at the arch foot under large earthquakes; the maximum acceleration and displacement responses of the grotto body are 3.94 m/s² and 13 mm respectively under small earthquakes; these values reach 18.41 m/s² and 66 mm under large earthquakes. In light of the numerical simulation results, three recommendations are proposed. Attention should be given to the seismic responses of the vulnerable parts of the grottoes. Moreover, vibration monitoring and long - term stability monitoring of the grottoes should be strengthened. These suggestions are intended to provide technical support for the preventive protection of the grottoes.

[1)] Graduate Student
[2)] Graduate Student
[3)] Professor
[4)] Professor
[5)] Professor

1. INTRODUCTION

In the midst of a rapidly evolving socio-cultural landscape, the notion of historical reverence has taken firm root in the collective consciousness, elevating heritage conservation to a central concern of our times. Throughout the lengthy process of historical development, rock formations have been subjected to the relentless forces of nature, including weathering, water and salt erosion, seepage, and microbial activity (Duan et al., 2018; Jiang Guo & Huang, 2021; Liu et al., 2020; Wang et al., 2018). These processes have led to deformation, slippage, and disintegration of certain rock masses, compromising the stability of grottoes. Consequently, the potential for seismic events poses one of the major threats to the stability of these structures. Approximately 70 percent of China's grottoes are located in earthquake-prone areas, with the majority constructed on precipitous mountain slopes (Shi, Fu & Wang, 2006). In such regions, even minor seismic events can cause serious damage to grottoes. Historical records indicate that the collapse of some grottoes in the Yungang, Dunhuang Mogao, Maijishan, and Tiantishan complexes are all related to seismic activity, highlighting the significant threat earthquakes pose to the stability of grottoes. Therefore, it is imperative to study the stability and seismic performance of grottoes.

Methods developed to assess stability or seismic response during earthquakes can be categorized into four general types: pseudo-static methods (Sun & Dias, 2019), Newmark methods (Aleksandra & Robert, 2021), probability analysis methods (Y. Wang, R. Wang & Zhang, 2021), and numerical simulation (Gaetano et al., 2021). Among these, numerical simulation has emerged as the most widely used method for stability analysis of rock masses in recent years (Yang et al., 2020). Studies by Shi, Fu & Wang (2006) revealed the seismic response patterns of two sections of the Mogao Grottoes. Borri & Grazini (2006) utilized 3D laser scanning and ANSYS to model Michelangelo's David and evaluate its stability under seismic activity in the Florence area. Sun & Wang (2012) employed FLAC 3D to analyze the seismic response of Xi'er Grottoes in Cave 19 of the Yungang Grottoes, demonstrating that shear failure is the predominant mode under seismic influence. Li, Du et al. (2018) obtained the seismic response of painted sculptures in the Mogao Grottoes through experiments and numerical simulation, identifying their vulnerable parts. Chen et al. (2020) analyzed the stress distribution and deformation characteristics of surrounding rock masses under tourist loads using a finite-difference method. Guo, Chen et al. (2020) used the same method to study the seismic response of the Mogao Grottoes under rare earthquakes, finding that shear failure was the main cause of damage.

For numerical simulation, the precision of the model is critical to the accuracy of the results (Scozzese et al., 2019). Traditional software used by most scholars for finite element model construction is time-consuming and lacks precision, often resulting in discrepancies between simulation outcomes and reality. With the advent of technologies such as 3D laser scanning, digital close-range photogrammetry, computer visualization, big data, and digital twins, cultural heritage protection has entered an era

of digitization and information technology (Li, Johari et al., 2019; Li, Xin et al., 2015; Feng et al., 2020). Reverse modeling of cultural relics based on point cloud data obtained from 3D laser scanning and digital close-range photogrammetry can generate accurate geometric information, providing a reliable basis for numerical simulation of cultural relics.

This paper presents a method for constructing finite element models for grottoes using 3D laser scanning technology to capture the three-dimensional point cloud data of grottoes and establish high-precision three-dimensional solid finite element models. To investigate the long-term stability and seismic performance of grottoes under the influence of earthquakes, we will analyze the stress distribution, plastic strain, deformation characteristics, and peak acceleration of grottoes under frequent and rare earthquake conditions. The results of this analysis are of great significance for seismic performance analysis, stability assessment, and the preventive protection of similar grottoes.

2. MATERIALS AND METHODS

2.1 Materials, Hardware Equipment, and Software

A specific cave, characterized by a hoof-shaped plan, was selected as the prototype for reverse modeling. The cave dimensions are 12.5 meters in length (East-West, X-direction), 8.7 meters in width (South-North, Y-direction), and 15.2 meters in height (Z-direction). The Buddha statue within the cave measures 13.5 meters in length, and the window dimensions are 3.95 meters in length, 0.56 meters in width, and 5.0 meters in height. To acquire the point cloud data of the cave and Buddha, a handheld 3D laser scanner from Lecia was utilized. The subsequent finite element model was constructed using a suite of software tools, including Geomagic, CAD, ANSYS, Hypermesh, and ABAQUS.

2.2 Reverse Modeling of Finite Element Model

The reverse modeling process of the finite element model involves converting points into lines, connecting lines into planes, and assembling planes into a three-dimensional body. The model is then meshed and imported into finite element software for analysis. The technical workflow is illustrated in Figure 1.

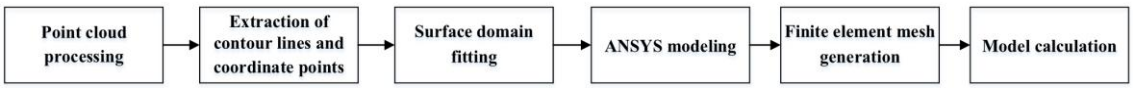

Fig. 1 Technical roadmap for reverse modeling of finite element model

2.2.1 Point Cloud Processing

The point cloud processing was conducted in two stages: point cloud encapsulation and mesh repair (Zhe et al., 2013). Initially, Geomagic was employed to encapsulate the denoised point cloud, with the maximum number of triangles set to 1.5 times the number of points. Subsequently, the encapsulated model was refined using Geomagic's "Mesh Doctor" tool to eliminate sharp edges and fill model defects with the "Fill Single" function. The processed model is depicted in Figure 2a.

2.2.2 Extraction of Contour Lines and Coordinate Points

The "Curve" function in Geomagic was utilized to extract contour lines and coordinate points from the refined model. The X-Y plane was used as the section, with the Z direction as the position degree and a spacing of 0.5 meters to intercept the contour lines of the cave surface, as shown in Figure 2b. Points were then created on the contour lines at 0.1-meter intervals, and the coordinate points were saved as a DXF file compatible with CAD software.

2.2.3 Surface Domain Fitting

The DXF file was imported into CAD, where the "Spline" function was used to connect coordinate points within the same height range to generate plane domains. To ensure closure of the domains, boundary lines were created on both sides and behind the point cloud model, forming closed curves within the same height range, as shown in Figure 2c. The generated domains were saved as a SAT file compatible with ANSYS.

2.2.4 ANSYS Modeling

The SAT file was imported into ANSYS, and the model was constructed using the "point - line - surface - body" method. Curves were used to connect endpoints at the same height, and the corresponding curves on the upper and lower surfaces were connected vertically. Six surfaces within the same height unit were then assembled into a solid entity, as shown in Figure 2d. Similar procedures were followed to join entities within multiple height units, and all entities were combined into a single entity using boolean operations. The entity model was saved as an IGES file compatible with Hypermesh.

2.2.5 Finite Element Mesh Generation

Given the complexity of the grotto geometry, meshing directly in ANSYS was challenging. Hypermesh was therefore used for preprocessing, offering robust meshing capabilities and compatibility with multiple finite element software interfaces. The element type was selected with care to ensure accurate calculation results. Due to the complex topology of the grotto and Buddha statue, hexahedral elements were avoided to prevent mesh degradation, which could affect convergence. Instead, element sizes of 1 meter for the grotto and 0.3 meters for the Buddha were chosen, resulting in a total of 111,825 meshes (Figure 2e). Mesh files were saved as INP files compatible with A.

2.2.6 Model Calculation

ABAQUS is renowned for its robust capabilities in solving nonlinear geotechnical problems. Compared to ANSYS, ABAQUS often exhibits better convergence during calculations. It offers a variety of geotechnical constitutive models (Bruschi et al., 2021), and its multi-load step settings more closely mimic real-world conditions.

The INP file, generated in the previous steps, was imported into ABAQUS for assembly. A cuboid was positioned at the base of the grotto to simulate the foundation, as depicted in Figure 2f. The detailed parameter settings for the ABAQUS calculations are outlined in Section 2.3.

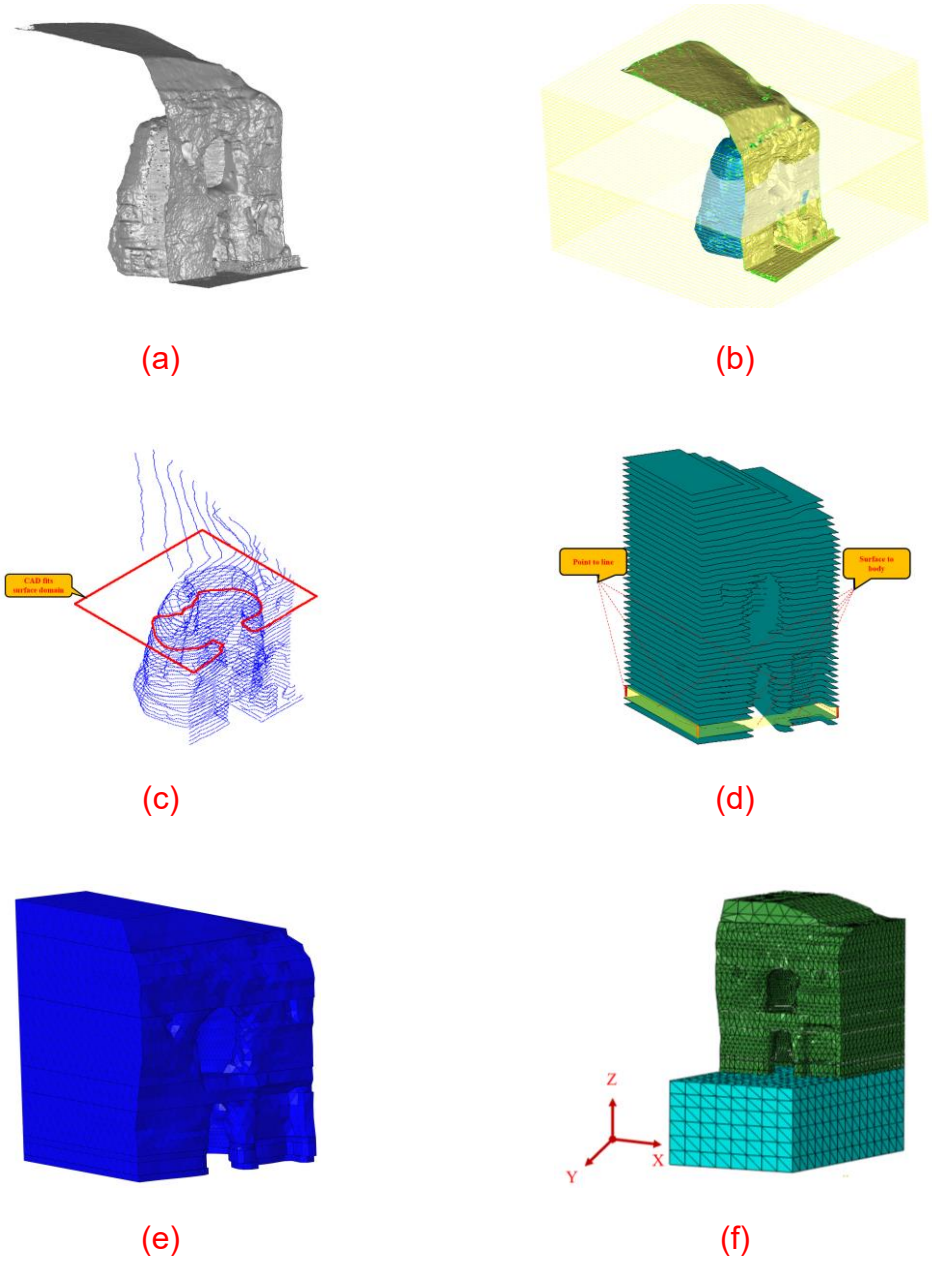

Figure 1. The process of reverse modeling of finite element model, (a) Point cloud processing, (b) Extraction of contour lines and coordinate points, (c) Surface domain fitting, (d) ANSYS modeling, (e) Finite element mesh generation, (f) The finite element model.

2.3 The Settings of Finite Element Model

2.3.1 Selection of Seismic Waves

In accordance with the provisions of the Chinese Code for Seismic Design of Buildings, the seismic precautionary intensity for the region housing the grottoes is categorized as degree Ⅶ. The design parameters for ground motion include a basic

acceleration of 0.15g, a design earthquake group of the 2nd category, and a site classification of class Ⅰ. For this simulation, the peak accelerations of the seismic events are set at 0.12g and 0.72g, corresponding to frequent earthquakes (with a 63.5% probability of exceedance in 50 years) and rare earthquakes (with a 2% probability of exceedance in 50 years), respectively.

To simulate these seismic conditions, the Taft (1952, Taft Lincoln School) and Santa Barbara (1952, Santa Barbara Courthouse) seismic waves were selected from the PEER NGA WEST strong earthquake database. Using these ground motion parameters and the target-spectrum fitting method, artificial seismic waves were synthesized. Additionally, the selected seismic waves underwent three processing steps: filtering, baseline correction, and amplitude modulation (Park & Kishida, 2019). The processed seismic waves are illustrated in Figure 3.

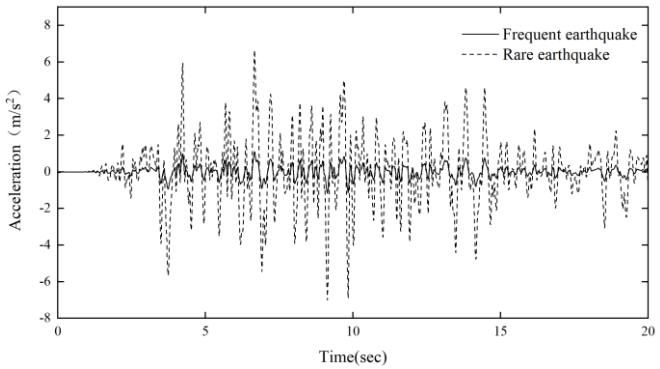

(a)

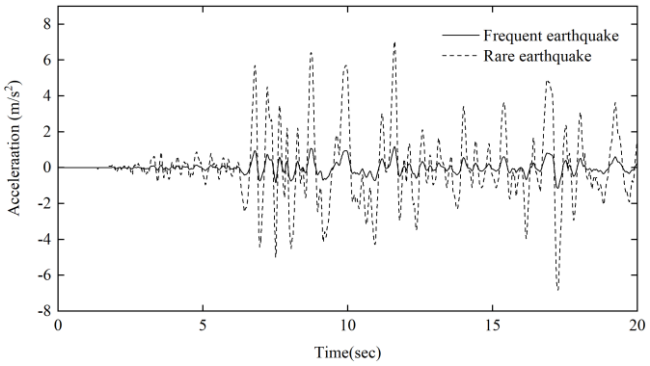

(b)

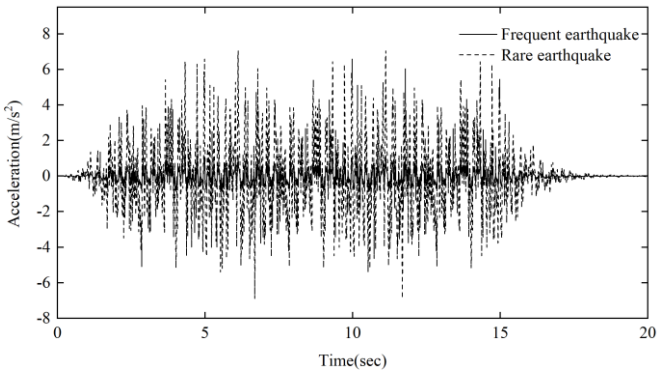

(c)

Figure 2. The adjusted acceleration time history curve, (a) Taft, (b) Santa, (c) Artificial seismic wave.

2.3.2 Material Properties

The physical and mechanical properties of the materials used in the model were determined based on relevant experiments and literature on grottoes. These properties are summarized in Table 1. It is also essential to consider damping during seismic analysis, although accurately determining structural damping can be challenging. In this study, Rayleigh damping was employed for assessment, which is defined as follows (Rahman & Gupta, 2020):

(1)

$$\xi=\frac{1}{2}\left(\frac{\alpha}{\omega_b}\right)+\frac{1}{2}\beta\omega_b$$

(2)

Where ξ represents the modal damping ratios, with a value of 0.05. α and β are the mass and stiffness damping coefficients, respectively. ω_a and ω_b are the first two natural frequencies.

ABAQUS is used to calculate the first two circular frequencies of the model, whose value are 18.46 and 60.31, respectively. According to formula (1) (2), the α and β are calculated to be 1.41, 0.0013, respectively.

Table 1. Physical and mechanical properties of rock mass

Density ($kg \cdot m^{-3}$)	Young modulus (MPa)	Poisson ratio	Cohesive (MPa)	Friction angle (°)	Compressive strength (MPa)	Tensile strength (MPa)
2490	3494	0.22	1.0	32	30	10

2.3.3 Load and Boundary Conditions

The analysis considers three primary loading conditions: gravity, frequent earthquake, and rare earthquake. Gravity is applied as a global gravitational load, while frequent and rare earthquakes are simulated using seismic waves applied in the X-direction of the model.

In the static analysis, the grotto model is bound to the lower foundation platform. The upper boundary of the model is free, while the bottom boundary is fully constrained from moving in both horizontal and vertical directions. The two sides (east-west) of the model are constrained from moving in the X-direction, and the back boundary is constrained from moving in the Y-direction. The front boundary, which includes the platform part, is constrained from moving in the Y-direction.

During the seismic analysis, the boundary conditions remain the same as in the static analysis, with the exception that the constraints on the X-direction movement of the two sides (east-west) of the model are released to allow for lateral displacement during the simulated seismic events.

2.3.4 Mohr-Coulomb Criterion

The dynamic implicit module of ABAQUS is employed for the calculations, assuming that the materials in the model exhibit elastoplastic behavior. The Mohr-Coulomb criterion is utilized to assess rock mass failure, which is defined by the following equations (Bahmani, Abedi & Clarke, 2019; Li, Ma et al., 2006):

$$f_s=\sigma_1-\sigma_3 N_\varphi+2c\sqrt{N_\varphi} \tag{3}$$

$$f_t=\sigma_3-\sigma^t \tag{4}$$

$$N_\varphi=\frac{1+\sin\varphi}{1-\sin\varphi} \tag{5}$$

Where σ_1 is the maximum principal stress, σ_3 is the minimum principal stress, φ is the friction angle, c is the cohesive force, and σ_t is the rock tensile strength.

According to the Mohr-Coulomb criterion, shear failure will occur in the rock mass if:

$$\sigma_1-\sigma_3\tan\varphi+c\geq\sigma_t \tag{6}$$

Alternatively, tensile failure will occur if:

$$\sigma_1-\sigma_3\tan\varphi+c\leq\sigma_t \tag{7}$$

These equations are critical for determining the failure modes of the rock mass under the applied loads, whether due to shear or tensile stresses.

3. RESULTS AND DISCUSSION

3.1 Static Results and Discussion

Figure 4a presents the Mises stress distribution within the grotto model under the influence of gravitational forces. The analysis indicates that the highest stress concentration is located at the arch foot of the grotto, with a value of 3.038 MPa. Furthermore, the arch foot, the rock mass flanking the window, the base of the Buddha statue, and the aisle exhibit significantly higher stress levels than other areas, suggesting localized stress concentrations. Based on experimental and literature data on grotto materials, the compressive strength of the grotto is 30 MPa. Therefore, the stress observed in each part of the grotto is substantially lower than its material strength, confirming that the grotto remains in a safe state under gravitational loads. Figure 4b illustrates the deformation pattern of the grotto, with the maximum deformation occurring at the apex, measuring 3.343 mm.

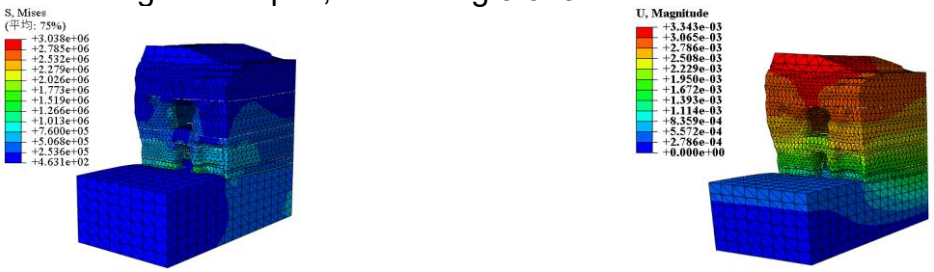

(a) (b)

Figure 3. Stress and displacement nephogram of grottoes, (a) Mises stress nephogram, (b) Displacement nephogram.

3.2 Seismic Response Results and Discussion

In accordance with the Code for Seismic Design of Buildings, the calculated results from the three seismic waves are suitable for the envelope analysis of the time-history method. To facilitate the analysis of seismic response, three monitoring points were selected on the grotto, as depicted in Figure 5. Points A1, A2, and A3 are located at the top of the platform, the Buddha statue, and the grotto, respectively.

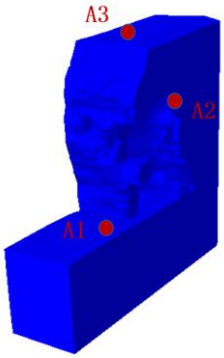

Figure 4. Layout of monitoring points

3.2.1 Stress and Strain

Figure 6a illustrates the plastic strain distribution within the grotto model under seismic conditions. Under frequent earthquake scenarios, no plastic deformation is observed in the grotto model, indicating that the grotto remains undamaged. Conversely, under rare earthquake conditions, plastic deformation occurs in the window, arch foot, rock mass on the east side, aisle, and base of the Buddha statue, suggesting that these areas have been compromised.

To investigate the failure mode of the grotto under seismic influence, the Mohr-Coulomb criterion was employed, and formulas (3) to (5) were utilized for assessment. Figures 6b and 6c depict the distribution of the maximum and minimum principal stresses, respectively. The maximum stress in most areas of the grotto is negative (compressive), while the minimum stress is positive (tensile). Consequently, fs is generally less than zero, indicating shear failure in these areas. When the minimum stress is tensile, its maximum value is 8.659 MPa, which is less than the tensile strength of the grotto. Thus, ft is less than zero, and no tensile failure occurs. In summary, the primary damage to the grotto is attributed to shear failure rather than tensile failure.

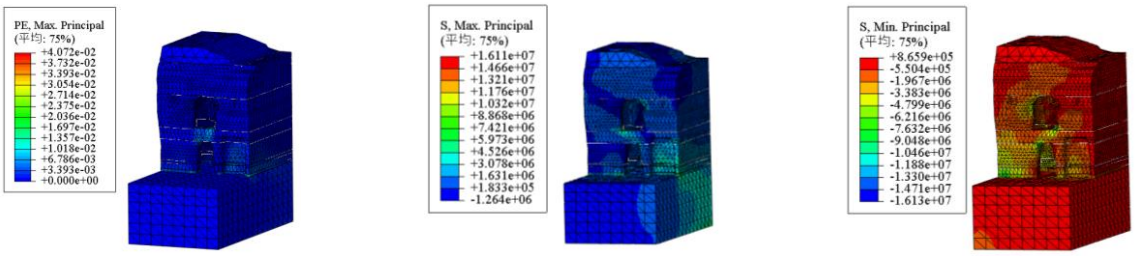

(a) (b) (c)

Figure 5. Stress and strain of grotto under rare earthquake, (a) Distribution of plastic strain, (b) The maximum principal stress, (c) The minimum principal stress.

3.2.2 Acceleration

Figures 7a and 7b display the time-history curves of acceleration in the X-direction for the monitoring points under seismic conditions. The acceleration of the monitoring points fluctuates with time, reaching peak values at 3.8s, 6.7s, 8.2s, 9.9s, 11.1s, and

12.6s, corresponding to the input motion. Under frequent earthquake conditions, the maximum acceleration of the grotto model is 3.94 m/s², an amplification compared to the input of 1.176 m/s². Under rare earthquake conditions, the maximum acceleration is 18.41 m/s², amplified from an input of 7.056 m/s².

An analysis of the three monitoring points reveals that the rock mass significantly amplifies the input motion, with response acceleration increasing gradually with elevation. This is attributed to the complex topological relationship of the grotto, featuring multiple free faces that cause seismic waves to reflect and superimpose within the rock mass, enhancing the amplification effect. Consequently, it is imperative to enhance the frequency of daily inspections of the grotto and implement continuous monitoring of grotto acceleration when necessary.

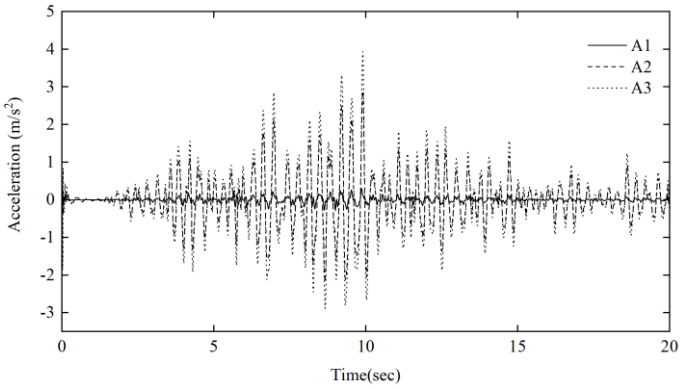

(a)

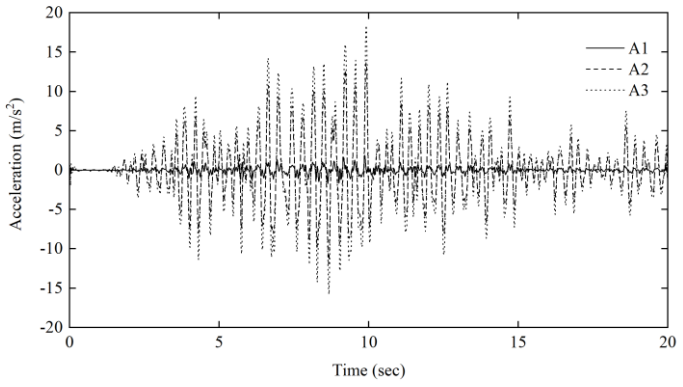

(b)

Figure 6. Time-history curve of acceleration in X - direction of monitorings point under the effect of earthquake, (a) Frequent earthquake, (b) Rare earthquake.

3.2.3 Displacement

Figures 8a and 8b depict the time-history curves of displacement in the X-direction for the monitoring points under seismic conditions. The response displacement of each monitoring point increases progressively with elevation. Under frequent earthquake conditions, the displacement of monitoring points exhibits fluctuations with time,

reaching peak values at 3.8s, 6.7s, 8.2s, 9.9s, 11.1s, and 12.6s, which correspond to the input motion. The maximum displacement of the grotto model is 8.3 mm, occurring at the top. Under rare earthquake conditions, peak displacements are observed at 3.8s, 6.7s, 8.2s, and 9.9s, corresponding to the input motion. However, after 9.9s, the time-history curve of displacement predominantly exhibits a negative trend, indicating that the grotto has been compromised under the influence of rare earthquake conditions, leading to a reversal in the direction of displacement.

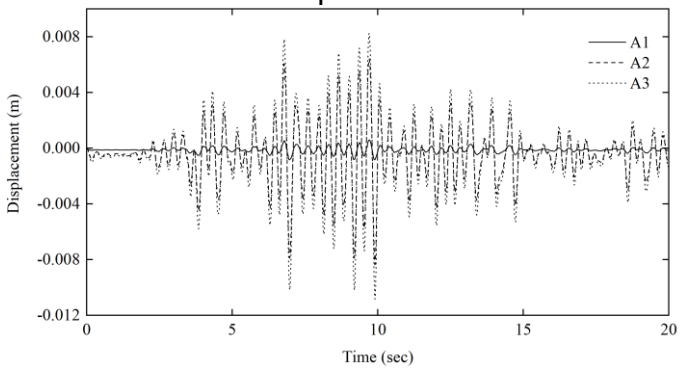

(a)

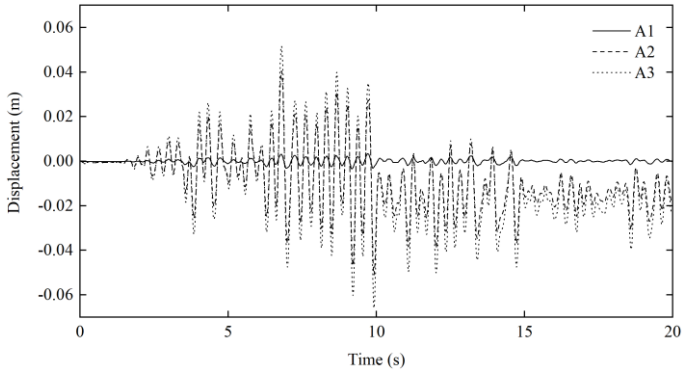

(b)

Figure 7. Time-history curve of displacement in X - direction of monitoring points under the effect of earthquake, (a) Frequent earthquake, (b) Rare earthquake.

3.2.4 Comparison and Analysis

reveals several key characteristics, as depicted in Figure 9, which illustrates the variation trends of response acceleration and displacement at each monitoring point under both working conditions.

1. The stress within the grotto increases proportionally with the amplitude of the input seismic motion.
2. The primary mode of damage to the grotto under seismic conditions is shear failure, as evidenced by the plastic strain distribution and the Mohr-Coulomb criterion analysis.
3. The degree of plastic deformation within the grotto is directly related to the

amplitude of the input seismic motion. Under frequent earthquake conditions, the absence of plastic deformation indicates no significant damage to the grotto. In contrast, under rare earthquake conditions, plastic deformation is observed in critical areas such as the window, arch foot, and the lower rock mass on the east side, suggesting localized damage.

4. The response acceleration and displacement of the grotto exhibit a linear relationship with the amplitude of the input seismic motion. The maximum acceleration during rare earthquake conditions is 4.67 times that observed during frequent earthquake conditions, while the maximum displacement is 6 times greater. This amplification effect highlights the vulnerability of the grotto to more intense seismic events.

In conclusion, the grotto's response to seismic events is characterized by a direct correlation between input motion amplitude and stress levels, a propensity for shear failure under seismic loading, and a progressive increase in plastic deformation with increasing seismic intensity. The findings emphasize the necessity of considering both frequent and rare earthquake scenarios in seismic safety assessments for grottoes, as the latter can lead to more severe and potentially catastrophic damage.

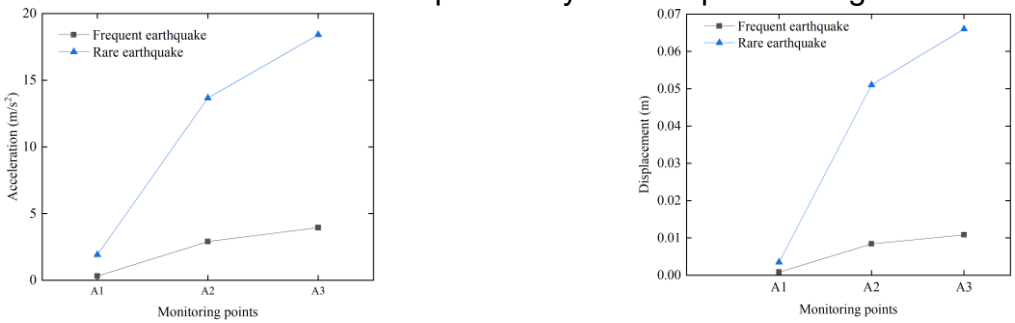

(a) (b)

Figure 8. Comparison diagram of dynamic response under different working conditions, (a) Peak acceleration, (b) Peak displacement

4. MONITORING SUGGESTIONS FOR GROTTOES

In recent years, numerous heritage sites featuring grottoes have established cultural relic protection units, which serve as platforms for the preservation, research, and exhibition of these invaluable sites, as well as for the monitoring of their condition. The development of finite element models not only aids in evaluating the stability of grottoes but also provides critical data and technical support for ongoing monitoring efforts. Based on the findings of this study, the following three recommendations are proposed for the daily monitoring of grottoes.

4.1 Enhanced Long-Term Stability Monitoring

It is imperative for cultural relic protection units to reinforce the long-term stability monitoring of grottoes. The numerical simulations conducted in this study indicate that grottoes maintain stability under gravitational and frequent earthquake conditions. However, under the impact of rare earthquakes, plastic deformation is observed in

critical areas such as the window, arch foot, rock mass on the east side, aisle, and base of the Buddha statue, leading to plastic failure. Field investigations have revealed the presence of visible cracks on the walls and ceiling of grottoes, with rock mass exhibiting potential instability due to fracture cutting and free action. To monitor the progression of these cracks, crack sensors should be installed in the existing fissures. Additionally, Total Station and 3D laser scanners can be employed to monitor deformation through the establishment of observation points on rock walls, the top of the Buddha statue, and other strategic locations. Stress and strain gauges can be placed in vulnerable areas such as the window, arch foot, east rock mass, aisle, and base of the Buddha to monitor stress development. The establishment and operation of a comprehensive grotto stability monitoring system will facilitate the integration and timely feedback of monitoring information, enabling early hazard identification and prediction, and the rapid formulation of prevention and control strategies. This is of paramount importance for disaster mitigation and the long-term preservation of heritage sites.

4.2 Focus on Vulnerable Parts under Seismic Influence

Attention should be directed towards the seismic response of vulnerable parts of grottoes. The numerical simulations highlight stress concentration and plastic deformation in the arch foot, window, rock mass on both sides, aisle, and base of the Buddha statue, which can lead to rock mass instability. Additionally, rock falls are observed in the cave tunnel and the ground beneath the window. To assess the weathering degree of rock mass in key areas, roughness instruments can be utilized. The damage degree and strength of vulnerable parts can be evaluated using rebound testers and ultrasonic technology, providing essential data for health monitoring, reinforcement, and maintenance of grottoes in the future.

4.3 Strengthened Vibration Monitoring

Cultural relic protection units should also enhance vibration monitoring caused by both seismic events and human activities. The numerical simulations indicate that the top of the grotto experiences significant acceleration and displacement responses, with maximum values reaching 18.41 m/s² and 0.066 m, respectively. Under rare earthquake conditions, plastic deformation in the window, arch foot, east rock mass, aisle, and base of the Buddha statue results in permanent damage to the grottoes. To investigate the propagation of seismic (vibration) effects on grottoes and their impact on stability, it is recommended to install wireless vibration sensors at the bottom and top of grottoes, the base of the Buddha statue, and the crown. To minimize damage to the grottoes during instrument installation, sensors should be secured at monitoring points using fitting techniques. It is suggested that subsequent work be based on field monitoring, including dynamic stability analysis and calculations for key objects, analysis of internal force variation rules under dynamic loads, identification of potential danger surfaces for internal damage, and the provision of theoretical support for hazard control and cultural relic preservation.

5. CONCLUSIONS

This study has successfully achieved the reverse modeling of grottoes utilizing 3D laser scanning data, simulating their structural response under three distinct working conditions: gravity, frequent earthquakes, and rare earthquakes. Furthermore, it has proposed several monitoring recommendations for grotto preservation. The following key conclusions are drawn:

1. The reverse modeling of grottoes using point cloud data from 3D laser scanning, in conjunction with software such as Geomagic, CAD, ANSYS, Hypermesh, and ABAQUS, has enabled the creation of a fine model and finite element analysis. The simulation results correlate well with the actual conditions of the grottoes, demonstrating the feasibility of this reverse modeling approach.
2. ABAQUS software has been employed to simulate the structural response of grottoes under the aforementioned conditions. The findings reveal that grottoes remain stable under gravitational loads. Under seismic conditions, shear failure is the predominant failure mode. While no plastic deformation is observed in grottoes under frequent earthquakes, plastic deformation occurs in the window, arch foot, east rock mass, aisle, and base of the Buddha statue under rare earthquake conditions. The plastic damage increases progressively with the amplitude of the input earthquake, leading to a corresponding increase in stress, response acceleration, and response displacement of the grotto.
3. The stability of grottoes necessitates ongoing monitoring and research. Based on the current state and numerical simulation of the grottoes, three protective measures have been suggested: (1) Cultural relic protection units should enhance long-term stability monitoring of grottoes. (2) Special attention should be given to the seismic response of vulnerable parts of grottoes. (3) Vibration monitoring caused by seismic events and human activities should be intensified.

Despite the advancements made in this study, several areas require further investigation. The selection of point cloud data is not limited to 3D laser scanning; alternative sources such as Total Station, close-range photogrammetry, UAV telemetry, and others are also viable. The simulation of grottoes currently does not account for the influence of fissures, seepage, and initial ground stress, which may introduce some inaccuracies. In ABAQUS dynamic simulations, the proportionality coefficient of Rayleigh damping is calculated based on empirically derived rock mass damping ratios, which may not guarantee the highest level of accuracy. Additionally, the rationality of dynamic boundary conditions in seismic simulations could be improved to better align with real-world scenarios. These aspects represent opportunities for future research and refinement of the modeling and analysis techniques for grotto preservation.

REFERENCES

Aleksandra, K., and J. Robert (2021). “Extended Newmark method to assess stability of slope under bidirect3.ional seismic loading.” *Soil Dyn. Earthq. Eng.*, 143: 106600.

Borri, A., and A. Grazini. (2006). “Diagnostic analysis of the lesions and stability of Michelangelo’s David.” *J. Cult. Herit.*, 7(4): 273–285.

Bahmani, B., R. Abedi, and P. L. Clarke. (2019). “A Stochastic Bulk Damage Model Based on Mohr-Coulomb Failure Criterion for Dynamic Rock Fracture.” *Appl. Sci.*, 9(5): 830.

Bruschi, G. J., F. Fante, M. T. Araújoet, G. D. Macedo, and C. A. Ruver. (2021). "Analysis of different failure criteria to evaluate bauxite tailings mechanical behavior through numerical modelling." *Soils Rocks.*, 44(1): e202105372.

Chen, W. W., Z. Q. Guo, J. K. Zhang, F. G. He, L. X. Zhang, Q. L. Guo and Q. Q. Pei. (2018). "Evaluation of Long-Term Stability of Mogao Grottoes Caves under Enhanced Loading Conditions of Tourists." *J. Perform. Constr. Facil.*, 32(4): 04018048.

Duan, Y. D., F. S. Wu, W. F. Wang, J. D. Gu, Y. F. Li, H. Y. Feng, T. Chen, G. X. L and L. Z. An. (2018). "Differences of Microbial Community on the wall paintings preserved in situ and ex situ of the Tiantishan Grottoes, China." *Int. Biodeterior. Biodegrad.*, 132: 102-113.

Feng, J., T. H. Meng, Y. H. Lu, J. G. Ren, G. Z. Zhao, H. M. Liu, J. Yang and R. Hong. (2020). "Nondestructive Testing of Hollowing Deterioration of the Yungang Grottoes Based on THz-TDS." Electronics., 9(4): 625.

Gaetano, F., N. Giuseppe, M. Federico, M. Amerigo, A. Gianluca, P. Edoardo and M. Mas. (2021). "Effect of Base Conditions in One-Dimensional Numerical Simulation of Seismic Site Response: A Technical Note for Best Practice." *GeoHazards.*, 2(4): 430-441.

Guo, Z. Q., W. W. Chen, J. K. Zhang, F. G. He, Q. L. Guo and X. D. Wang. (2020). "Seismic responses of the densely distributed caves of the Mogao Grottoes in China." *Bull. Eng. Geol. Environ.*, 80(2): 1335-1349.

Jiang, G. H., F. Guo, and J. Z. Huang. (2021). "Acceleration and mitigation of sandstone weathering in the Yungang Grottoes for more than one millennia." *Z. Geomorphol.*, 62(3): 301-314.

Li, H. B., X. D. Ma, J. R. Li, H. C. Dai and K. Q. Xiao. (2006). "Study on influence factors of rock cavern displacement under earthquake." *Chin. J. Geotech. Eng.*, 28(03): 358-362. (in Chinese)

Liu, H. L., X. D. Wang, Q. L. Guo, M. Q. Zhang and Y. W. Wang. (2020). "Experimental investigation on the correlation between rainfall infiltration and the deterioration of wall paintings at Mogao Grottoes, China." *Bull. Eng. Geol. Environ.*, 79(5): 1199-1207.

Li, L. S., J. G. Du, H. L. Liu, R. H. Chen and T. Liu. (2016). "Dynamic characteristics and seismic responses of painted sculptures of Dunhuang Mogao Grottoes." *J. Cult. Herit.*, 22:1040-1048.

Li, X. S., M. Y. M. Johari, H. S. Wue and P. Velu. (2021). "The Use of Digital Advancement Technology in Protecting the Longmen Grottoes Art." *J. Phys. Conf. Ser.*, 1875(1): 012011.

Park, D. S. and T. Kishida. (2019). "Seismic Response of Embankment Dams Based on Recorded Strong-Motion Data in Japan." *Earthquake Spectra.*, 35(2): 955-976.

Ministry of Housing and Urban-Rural Development of the People's Republic of China and General Administration of Quality Supervision, Inspection and Quarantine of the People's Republic of China. (2016). Code for Seismic Design of Buildings. Published by China Building Industry Press. (in Chinese)

Rahman, H. M. and C. Gupta. (2020). "Computation of Rayleigh damping coefficient of a rectangular submerged floating tunnel (SFT)." *SN Appl. Sci.*, 2(10): 91-98.

Sun, B. and N. B. Peng. (2012). Wang F R. “Seismic Dynamic Responses of No.19 Grotto's West Side Cave of Yungang Grottoes.” *J. Southwest Jiaotong Univ.*, 47(04): 573-579.

Scozzese, F., L. Ragni, R. Tubaldi and F. Gara. (2019). “Modal properties variation and collapse assessment of masonry arch bridges under scour action.” *Eng. Struct.*, 199(C): 109665-109665.

Shi, Y. C., C. H. Fu and L. M. Wang. (2006). “Numerical simulation analysis of mechanism of seismic deformation damage of country rock of grottoes.” *Rock Soil Mech.*, 27(04): 543-548.

Sun, Q. Q. and D. Dias. (2019). “Assessment of stress relief during excavation on the seismic tunnel response by the pseudo-static method.” *Soil Dyn. Earthq. Eng.*, 117: 384-397.

Wang, K. P., X. Guang, S. T. Li, et al. (2018). “Geo-environmental characteristics of weathering deterioration of red sandstone relics: a case study in Tongtianyan Grottoes, Southern China.” *Bull. Eng. Geol. Environ.*, 77(4): 1515-1527.

Wang, Y. X., R. Wang and J. M. Zhang. (2021). “Large-scale seismic seafloor stability analysis in the South China Sea.” *Ocean Eng.*, 235: 109334.

Yang, J. C., K. W. Liu, X. D. Li and Z. X. Liu. (2020). “Stress initialization methods for dynamic numerical simulation of rock mass with high in-situ stress.” *J. Cent. South Univ.*, 27(10): 3149-3162.

Zhang, L. and Y. W. Xin. (2015). “The Establishment of IOT Based System in Conservation and Utilization of Mogao Grottoes.” *AMM.*, 3822(740): 1011-1018.

Zhe, L., H. L. Y. Xiang, Li Z Q, B. A. Han and J. J. Huang. (2013). “The Research of Reverse Engineering Based on Geomagic Studio.” *AMM.*, 2555(365-366): 133-136.